

**Topological node-line semimetal in three-dimensional graphene networks**Hongming Weng,<sup>1,2,\*</sup> Yunye Liang,<sup>3</sup> Qiunan Xu,<sup>1</sup> Rui Yu,<sup>4</sup> Zhong Fang,<sup>1,2</sup> Xi Dai,<sup>1,2</sup> and Yoshiyuki Kawazoe<sup>3,5</sup><sup>1</sup>*Beijing National Laboratory for Condensed Matter Physics, and Institute of Physics, Chinese Academy of Sciences, Beijing 100190, China*<sup>2</sup>*Collaborative Innovation Center of Quantum Matter, Beijing, China*<sup>3</sup>*New Industry Creation Hatchery Center, Tohoku University, Sendai 980-8579, Japan*<sup>4</sup>*International Center for Materials Nanoarchitectonics (WPI-MANA), National Institute for Materials Science, Tsukuba 305-0044, Japan*<sup>5</sup>*Thermophysics Institute, Siberian Branch, Russian Academy of Sciences, Russia*

(Received 15 January 2015; revised manuscript received 20 May 2015; published 8 July 2015)

Graphene, a two-dimensional (2D) carbon sheet, acquires many of its amazing properties from the Dirac point nature of its electronic structures with negligible spin-orbit coupling. Extending to 3D space, graphene networks with negative curvature, called Mackay-Terrones crystals (MTCs), have been proposed and experimentally explored, yet their topological properties have yet to be discovered. Based on the first-principle calculations, we report an all-carbon MTC with topologically nontrivial electronic states by exhibiting node lines in bulk. When the node lines are projected onto surfaces to form circles, “drumhead”-like flat surface bands nestled inside of the circles are formed. The bulk node line can evolve into a 3D Dirac point in the absence of inversion symmetry, the existence of which has been shown to be plausible in recent experiments.

DOI: [10.1103/PhysRevB.92.045108](https://doi.org/10.1103/PhysRevB.92.045108)

PACS number(s): 73.20.-r, 03.65.Vf, 71.20.-b, 73.43.-f

**I. INTRODUCTION**

Carbon is one of the most fascinating elements in nature. It can form many different crystal structures with diverse electronic properties, such as C<sub>60</sub> [1], nanotubes [2], graphene [3], graphite, and diamond. Among them, graphene is one of the most amazing materials. It supports the Dirac point in its low-energy electronic structure, described as  $H = v\vec{k} \cdot \vec{\sigma}$ , where  $v$  is the velocity,  $\vec{k} = (k_x, k_y)$  is the momentum, and  $\vec{\sigma}$  is the Pauli matrix. This novel electronic state leads to many interesting phenomena, such as the unconventional quantum Hall effect, large magnetoresistance, and unusual optical properties, all of which make graphene potentially useful [4]. The presence of a two-dimensional (2D) Dirac cone is fragile, and two conditions are required to protect it: (i) the absence of spin-orbit coupling (SOC), and (ii) the presence of inversion symmetry. The first condition is naturally satisfied in graphene, because its SOC strength is negligible ( $\sim 10^{-3}$  meV) [5]. Nevertheless, if sufficiently strong SOC is introduced in graphene in a proper way, a gap at the Fermi level will be opened, which would lead to a quantum spin Hall insulator (i.e., a 2D topological insulator) [6]. The second requirement is, however, very strong, and it is satisfied only in the presence of *A-B* sublattice symmetry, which can be easily broken, leading to a normal insulating state, similar to that in a BN nanosheet.

As proposed by Mackay and Terrones [7], graphene can be extended to 3D space to form 3D networks by placing graphitic tiles consisting of four- to eight-membered rings onto the Schwarz minimal surface. Hereafter, we call such a 3D all carbon allotrope a Mackay-Terrones crystal (MTC). The Schwarz minimal surface is a 3D periodic minimal surface with its mean curvature  $H = (k_1 + k_2)/2$  being zero and its Gaussian curvature ( $K = k_1 k_2$ ) being negative everywhere on it. Here  $k_1$  and  $k_2$  are the principal curvatures. There are various Schwarz minimal surfaces, such as primitive (*P*),

diamond (*D*), and gyroid (*G*). One type of MTC based on a *P* surface is shown in Fig. 1. Different from C<sub>60</sub>-like fullerene, which has positive Gaussian curvature, a MTC has negative Gaussian curvature and is periodically connected. Such a 3D network of *sp*<sup>2</sup>-bonded carbon has unique properties, such as a high surface-to-volume ratio and remarkable porosity, which have stimulated extensive studies [8,9]. Theoretically, MTC has been proved to be dynamically stable and requires less formation energy than C<sub>60</sub> [10,11]. Experimentally, a saddlelike nanocarbon sheet, the main component of MTC, has been successfully synthesized [12]. Similar negatively curved *sp*<sup>2</sup> networks have been observed in spongy carbon [13] and a negative replica of zeolite [14]. Recently, high-quality 3D nanoporous graphene fabricated by using nanoporous Ni as a template showed a very similar MTC structure [15,16], making its synthesis very promising. On the other hand, the topological properties of the band structure for these all-carbon MTCs remain unexplored and will be the main subject of this paper. We will show that such all-carbon MTCs can host nontrivial electronic states, including topological node lines and 3D Dirac points, which are distinct from its 2D counter material graphene. Similar node lines have also been proposed in optimally tuned photonic crystal composed of gyroid [17], the Schwarz minimal *G* surface. Other proposed carbon systems include Bernal graphite [18,19] and a hyper-honeycomb lattice [20]. A carbon gyroid [21] is found to be metal with a Dirac cone in conduction bands farther away from the Fermi level. A node line was also proposed in a model of Dirac or Weyl superconductors [22].

**II. RESULTS**

We concentrate on the MTC formed with a Schwarz minimal *P* surface. As shown in Fig. 1, a stable structure with a simple-cubic lattice in the *Pm* $\bar{3}$ *m* space group, and 176 atoms per unit cell, has been obtained by Tagami *et al.* in Ref. [23] and labeled as 6-1-1-p. We have employed the software package OPENMX [24] for the first-principles calculation. It is based on a norm-conserving pseudopotential and pseudoatomic

\*hmweng@iphy.ac.cn

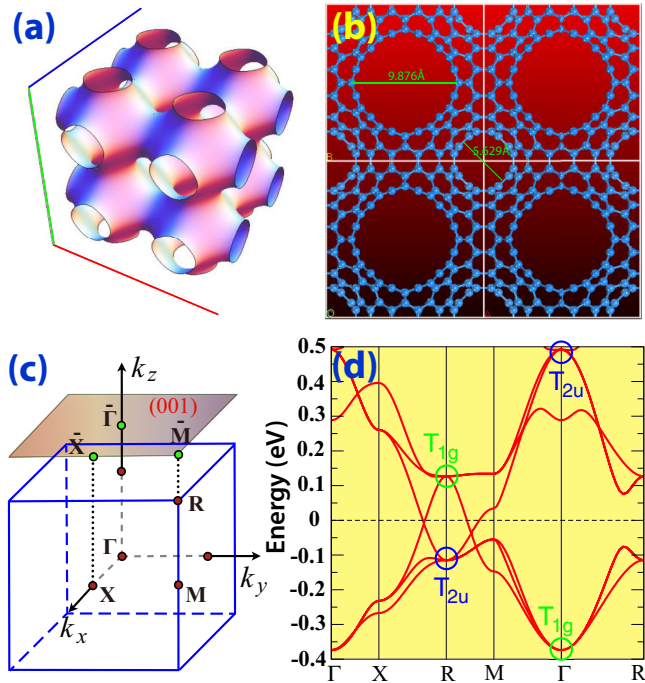


FIG. 1. (Color online) (a) The Schwarz minimal  $P$  surface in a  $2 \times 2 \times 2$  supercell. (b) The top view of a 6-1-1-p MTC in a  $2 \times 2$  supercell. (c) Bulk and (001)-surface Brillouin zone, as well as the highly symmetrical  $k$  points. (d) Band structure from the first-principles calculation. The two triply degenerate eigenstates at  $\Gamma$  and  $R$  with  $T_{1g}$  and  $T_{2u}$  symmetrical representation are marked. The band inversion between them can be easily seen.

localized basis functions, which is highly efficient for the MTC with more than 100 atoms. The choice of pseudopotentials, pseudoatomic orbital basis sets C6.0-s2p2d1, and the sampling of a Brillouin zone with a  $10 \times 10 \times 10$  grid have been carefully checked. After full structural relaxation, we get the lattice constant  $a = 14.48 \text{ \AA}$ , and the diameters of the pipes or pores are around  $9.876$  and  $5.629 \text{ \AA}$ , respectively, which are in good agreement with the results from Ref. [23]. The electronic band structure of this crystal, calculated based on the local density approximation (LDA), is shown in Fig. 1(d). We find that this crystal is a semimetal with band crossings around the Fermi level, similar to the massless Dirac cone in graphene, but they are in fact very different—this is the key issue of this paper.

### A. Band structure

Detailed analysis of the band structure reveals the following: (i) The occupied and unoccupied low-energy bands are triply degenerate at  $\Gamma$ , and they have  $T_{1g}$  and  $T_{2u}$  symmetry, respectively. The representations of the eigen-wave-functions are obtained by calculating the eigenvalue of the symmetrical operators in the little group. Those of  $T_{1g}$  are even while those of  $T_{2u}$  are odd under spatial inversion symmetry. Moving away from the  $\Gamma$  point their degeneracy is lifted, but upon arriving at the  $R$  point their degeneracy is recovered again. However, their energy ordering exchanges, leading to the so called band inversion, which is one of the key ingredients for

the topological insulators [25,26]. Due to the band inversion, the band crossings happen along both  $X$ - $R$  and  $R$ - $M$  paths, as seen from Fig. 1(d). (ii) Including SOC in the first-principles calculation, a gap will open up around the band crossings, leading to a 3D strong topological insulator with a  $Z_2$  index of (1;111) [27] by treating the lower half of the anticrossing bands as occupied. However, similar to graphene, the computed SOC splitting is small (around  $0.13 \text{ meV}$  or  $1.5 \text{ K}$ ), and it can be neglected in cases with temperature higher than  $1.5 \text{ K}$ .

The low-energy bands near the Fermi level are formed by the overlapping of the molecular orbitals with  $T_{1g}$  and  $T_{2u}$  symmetry. If a single unit cell of this MTC is taken out, it becomes an isolated carbon cluster having approximately spherical symmetry. The MTC can be viewed as a cubic lattice of such a carbon cluster. The above molecular orbitals can be viewed as “atomic orbitals” with  $g$ - and  $f$ -wave symmetry under the cubic crystal field. For example, the  $T_{1g}$  sector consists of  $g_{xy}(x^2-y^2)$ ,  $g_{yz}(y^2-z^2)$ , and  $g_{zx}(z^2-x^2)$  orbitals, which are a subgroup of  $g$  orbitals split under a cubic crystal field. The  $T_{2u}$  sector contains  $f_{x(y^2-z^2)}$ ,  $f_{y(z^2-x^2)}$ , and  $f_{z(x^2-y^2)}$  orbitals from  $f$  orbitals. These can be easily found in a character table of point group symmetry in any textbook on group theory. Thus, these six hypothetical atomic orbitals are used as a basis set to reproduce the low-energy physics of this system. A Slater-Koster tight-binding (TB) Hamiltonian has been established, and the on-site energy levels, as well as hopping parameters, can be obtained by fitting the band structure from the first-principles calculations (see the Appendix A 1 for details). The triply degenerate  $T_{1g}$  and  $T_{2u}$  bands at  $\Gamma$  have eigenenergies of  $E_g + 4V_{ggp} + 2V_{ggd}$  and  $E_f - 4V_{ffd}$ , respectively. Those at  $R$  are  $E_g - 4V_{ggp} - 2V_{ggd}$  and  $E_f + 4V_{ffd}$  due to the nearest-neighbor hopping. Here,  $E_g$  and  $E_f$  are on-site energies for  $g$  and  $f$  orbitals.  $V_{ggp}$  and  $V_{ggd}$  are the hopping parameters among  $g$  orbitals.  $V_{ffp}$  and  $V_{ffd}$  are those for  $f$  orbitals. From these analyses, we learned that the band inversion or the switching of  $g$  ( $T_{1g}$ ) and  $f$  ( $T_{2u}$ ) orbitals between  $\Gamma$  and  $R$  points is due to the strong energy dispersion (or the large hopping parameters). As shown in Fig. 2, this TB model can well reproduce the lower energy bands, which are crucial to the band topology, with the

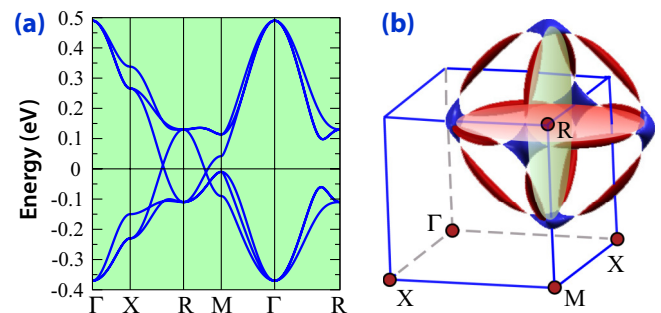


FIG. 2. (Color online) (a) Band structure from effective tight-binding model calculation, which reproduces all the features of Fig. 1(d). (b) The Fermi surface consists of three lotus-root-like rings. These rings are center the  $R$  point and are parallel to the  $k_x = \frac{\pi}{a}$ ,  $k_y = \frac{\pi}{a}$ , and  $k_z = \frac{\pi}{a}$  plane, respectively. They are formed by the electron pockets (blue) and hole pockets (red) connected by nodal points at the Fermi energy.

fitted Slater-Koster parameters (in eV)  $E_g = -0.12$ ,  $E_f = 0.19$ ,  $V_{ffp} = 0.019$ ,  $V_{ffd} = -0.075$ ,  $V_{fgp} = 0.05$ ,  $V_{fgd} = 0.0$ ,  $V_{ggp} = -0.035$ , and  $V_{ggd} = -0.055$ . The mean-square error is minimized to  $0.0016 \text{ eV}^2$  with sampling  $k$  points along the highly symmetrical path shown in Fig. 1(d). Artificially reducing the hopping parameters (such as by expanding the lattice parameter) by 50% will eliminate the band inversion, with  $T_{1g}$  states lower than the  $T_{2u}$  states at the  $R$  point. This calculation also suggests that the strength of band inversion in the system is strong.

### B. Topological node lines and 3D Dirac points

Interestingly, the band crossings in MTC lead to node lines rather than node points. In other words, the band crossings exist along certain closed loops in 3D momentum space, and they generate three circular-like node lines around the  $R$  point, as shown in Fig. 2. These node lines are protected by two factors: one is the coexistence of time reversal ( $T$ ) and spacial inversion ( $P$ ) symmetry, and the other is that the SOC is negligible.

With the coexistence of  $P$  and  $T$  symmetries, there exists a certain gauge choice under which the spinless Hamiltonian is completely real-valued (see the Appendix B for details). Now we will show that for this system, if there is an energy level crossing of two bands at a momentum  $\mathbf{k}_0$ , a stable node line will unavoidably appear. Around the crossing point, the two-level  $2 \times 2$  Hamiltonian can be written in the following general form:

$$\mathcal{H} = d_0(\vec{k}) + d_x(\vec{k}) \cdot \sigma_x + d_y(\vec{k}) \cdot \sigma_y + d_z(\vec{k}) \cdot \sigma_z, \quad (1)$$

where the Pauli matrices  $\sigma_i$  ( $i = x, y, z$ ) denote the two-band space. Without loss of generality,  $d_i(\vec{k})$  ( $i = 0, x, y, z$ ) are all real functions of  $\vec{k}$ . The eigenenergy of  $\mathcal{H}$  is

$$E(\vec{k}) = \pm \sqrt{d_x^2(\vec{k}) + d_y^2(\vec{k}) + d_z^2(\vec{k})} + d_0(\vec{k}), \quad (2)$$

and the energy degeneracy can be obtained when the three conditions  $d_i(\vec{k}) = 0$  ( $i = x, y, z$ ) are satisfied with three parameters  $\vec{k}(k_x, k_y, k_z)$  in 3D momentum space. As mentioned above, the Hamiltonian can be chosen to be real-valued, leading to  $d_y = 0$ . The remaining  $d_0(\vec{k})$ ,  $d_x(\vec{k})$ , and  $d_z(\vec{k})$  can be expanded around  $k_0$ , and the location of the crossing points can be determined by  $d_x(\vec{k}_0) \approx \delta_x + \vec{v}_x(\vec{k} - k_0) = 0$  and  $d_z(\vec{k}_0) \approx \delta_z + \vec{v}_z(\vec{k} - k_0) = 0$ , where  $\vec{v}_i = \vec{\nabla}_{\vec{k}} d_i(\vec{k})$  and  $\delta_i$  denote the small perturbative terms with both  $T$  and  $P$  symmetries. In the generic case, the above two equations give a line in the vicinity of  $k_0$  with its direction determined by  $\vec{v}_x \times \vec{v}_z$ . Therefore, the generic solution of the band crossing point in 3D  $k$  space is a closed loop. Any external perturbations that maintain  $T$ ,  $P$ , and translational symmetry can only shift or distort but not eliminate the nodal loops.

The topologically stable node line in MTC is only protected by  $P$  and  $T$ , and no other symmetry is required. The additional mirror symmetry in the present system only forces the node lines to stay in the  $k_z$  (or  $k_x, k_y$ ) =  $\frac{\pi}{a}$  plane. The cubic symmetry leads to three in-plane node lines, as was found from our calculations in Fig. 2. The node lines are not necessarily flat in energy, and they can have energy dispersion in the  $k$  space determined by the  $d_0(\mathbf{k})$  term (which breaks the particle-hole symmetry). In contrast with other proposals for

the topological node lines [28], the appearance of node lines in MTC is very stable and does not require fine tuning any parameters. This mechanism to generate topological node lines in three-dimensional materials only requires  $T$  and  $P$  symmetry and weak enough SOC, which can be easily applied to a large class of materials consisting of mainly the light elements.

It is now clear that this 3D MTC is different with graphene in the sense that it is a semimetal with node lines in the 3D momentum space with the presence of both  $T$  and  $P$  symmetries. The situation becomes even more interesting if  $P$  symmetry is broken further. In such a case, from the above discussions, we will generally expect three conditions  $d_i(\mathbf{k}) = 0$  with three parameters for the band crossing points, leading to isolated points in the 3D  $k$  space. This is merely the 3D Dirac metals discussed recently [29–34]. On the other hand, compared with other proposals for Dirac semimetals, the 3D Dirac point here is topologically stable and does not require protection from any crystalline symmetry. Similar to the situation in graphene, finite SOC will open a gap at the Dirac point, and it makes the system a topological insulator. In fact, although our calculated structure has inversion symmetry, most of the known real samples of MTC [15,16] have strong defects and orientation disorder, which should break inversion symmetry. The plausible existence of these stable 3D Dirac points has been indicated by the density of states [15] and heat capacity measurements [35]. If  $T$  symmetry is further broken in the system, we will expect Weyl semimetal states; this has been studied extensively but not realized yet experimentally [36–39].

### C. Fermi surface and surface flat band

The two crossing bands within the  $k_z = \frac{\pi}{a}$  plane obtained by the TB Hamiltonian are plotted in Fig. 3. In general, the crossing of bands does not happen at the same energy. They have energy dispersion around 25 meV. The alternative electron and hole pockets are formed when the band crossing is lower or higher than the Fermi level, and this results in a lotus-root-like Fermi surface instead of a dispersionless line.

This topologically stable node-line semimetal state can have nontrivial surface states [28,40–43]. For the (001) surface, the three node-line rings are projected to be a ring and

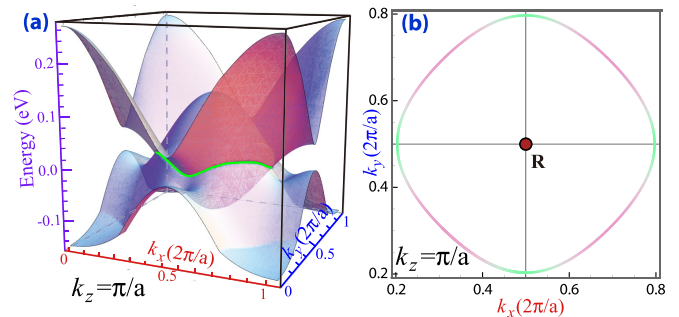


FIG. 3. (Color online) (a) Band crossings of the two bands near the Fermi level form node line (in green) in the  $k_z = \frac{\pi}{a}$  plane. (b) The crossing happens at different eigenenergies as indicated by different colors, where greener denotes lower in energy.

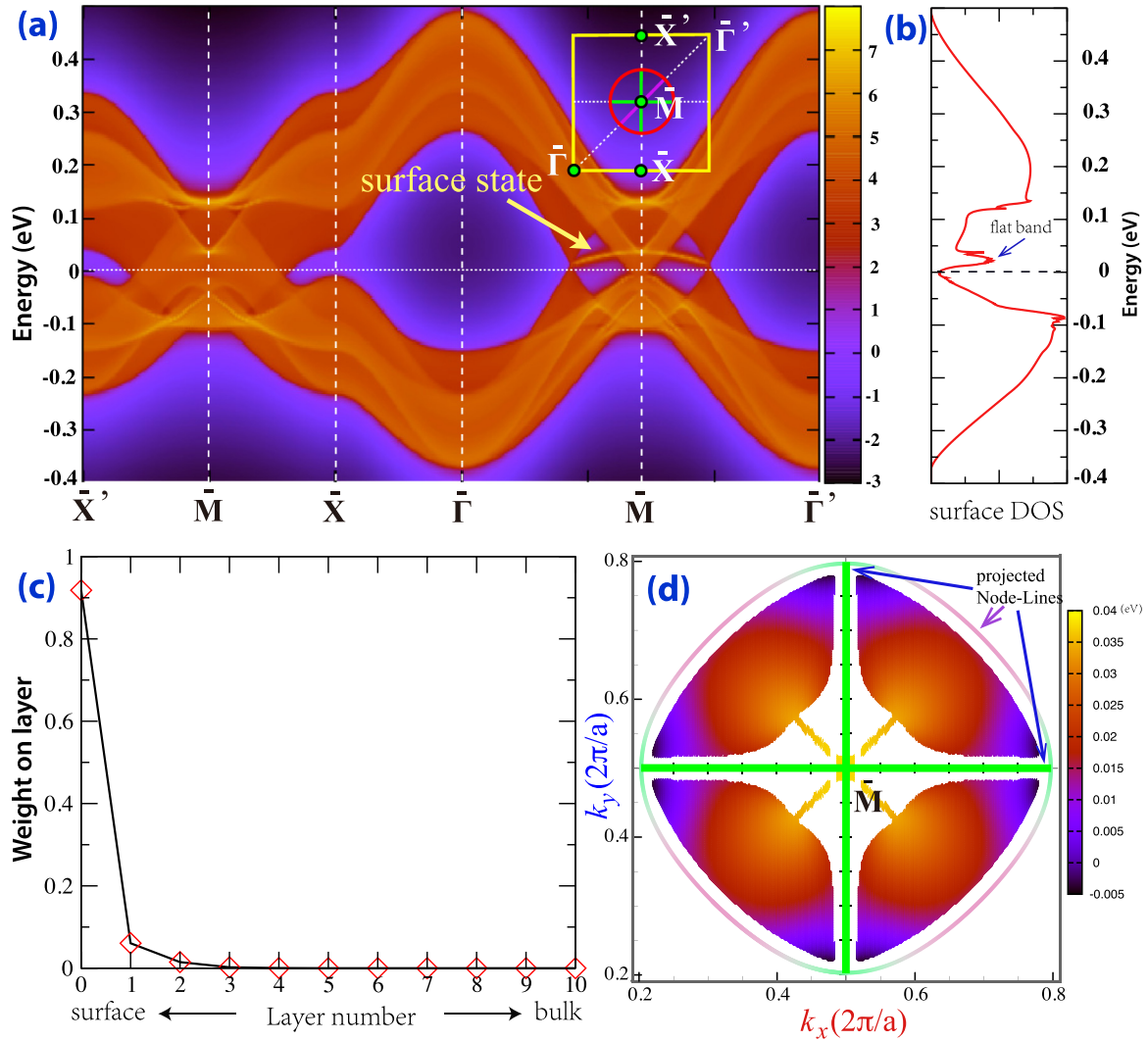


FIG. 4. (Color online) The (001)-surface state. (a) The nearly flat surface band is nestled between two solid Dirac cones, which are the projection of one of the node-line circles as indicated in the inset (red circle). The other two node-line rings are projected as two orthogonal diameters (green line). (b) The surface density of state. (c) The wave function of the surface state indicated by the arrow decays rapidly into bulk. (d) The eigenenergy distribution of a surface flat band nestled inside of a projected node-line circle, which looks like a vibration model of a “drumhead.” The mixing of surface and bulk states leads to discontinuity in this plot.

two orthogonal diameter segments inside of it, as shown in Fig. 4(a). The (001)-surface state is calculated based on the six-band TB model using both the Green’s function method and the slab-model method [44]. There is a nearly flat surface band nestled inside of the projected node-line ring with its bandwidth being about 40 meV due to the particle-hole asymmetry. The peaklike surface density of states contributed by this nearly flat band is clearly shown in Fig. 4(b), which is proposed to be an important route to high-temperature surface superconductivity [45,46]. The layer-resolved weight of the wave function for the surface flat band is shown in Fig. 4(c). It penetrates just three layers into the bulk with most of the weight on the surface layer. The surface localization of these flat bands is well resolved for those separated from bulk bands. The nestled flat surface states have small dispersion, and their eigenenergy distribution in the surface BZ is shown in Fig. 4(d), which looks like some vibrational mode of a “drumhead.” Such “drumhead”-like states are readily detected

by angle-resolved photoelectron spectroscopy or scanning tunneling microscopy.

The topological node-line state, as well as its surface flat band, can be understood by studying an effective  $2 \times 2$  toy model Hamiltonian. Taking  $d_x = k_z$ ,  $d_y = 0$ , and  $d_z = M - B(k_x^2 + k_y^2 + k_z^2)$ , the Hamiltonian gives a node line determined by  $k_x^2 + k_y^2 = \frac{M}{B}$  in the  $k_z = 0$  plane. Obviously  $\frac{M}{B} > 0$  is required. The topology of this effective continuum bulk Hamiltonian has been analyzed [47] (see the Appendix C for details) and found to have topologically protected (001) surface states with dispersionless zero eigenenergy inside of the projected node-line circle given by  $\bar{k}_x^2 + \bar{k}_y^2 = \frac{M}{B}$ . Here  $(\bar{k}_x, \bar{k}_y)$  denotes the  $k$  point in the (001) surface Brillouin zone. As mentioned above,  $d_0(\vec{k})$  determines the energy dispersion of the node line, as well as the surface flat band, though the detailed dispersion of surface states is also influenced by the surface potential in practice [44].

### III. DISCUSSION

We find that 6-1-1-p is not the only MTC having such a novel node-line semimetal state. The MTC with the structure labeled as 6-1-2-p [23] also has such a nontrivial topological state (as shown in the Appendix A 2). The differences are as follows: (i) The band inversion happens at the  $M$  point, and the  $Z_2$  index is (1;000) when even weaker SOC splitting (about 0.03 meV compared with 0.136 meV in 6-1-1-p) is considered. (ii) The low-energy physics around the Fermi level can be described by six atomiclike molecular orbitals also, but they are  $T_{1u}$  ( $p_x$ ,  $p_y$ , and  $p_z$ ) and  $T_{2g}$  ( $d_{xy}$ ,  $d_{yz}$ , and  $d_{xz}$ ). A similar tight-binding model on a simple-cubic lattice can also reproduce all of its electronic structure. (iii) There are also three mutually perpendicular node-line circles centering the  $M$  point instead of the  $R$  point. A similar surface state with a nearly flat band can also be obtained. Therefore, it is most plausible that there are more 3D MTCs that can host such a node-line semimetal state.

### IV. CONCLUSION

In summary, based on the first-principles calculations, we have predicted that a family of all-carbon 3D allotropes, namely Mackay-Terrones crystals, can have a nontrivial topological node-line semimetal state, which is protected by both time-reversal symmetry and inversion symmetry after band inversion. When such a bulk node line is projected onto a surface to form a circle, there are flat bands nestled inside of it. Such a ‘‘drumhead’’-like state is an ideal area for many interaction-induced nontrivial states, such as superconductivity and fractional topological insulator states. Furthermore, if inversion symmetry is broken, the node lines will evolve into stable 3D Dirac points. Two examples of such MTC with stable structure have been discussed. These predications will most probably be directly observable in further experiments.

*Note added.* During our review of this work, we noticed a similar work by Y. Chen *et al.* [48], in which the node line, the nestled nearly flat surface bands, and the stable 3D Dirac nodes due to inversion symmetry breaking proposed in this manuscript are also obtained for another carbon system. Other subsequently proposed candidate materials include  $\text{Ca}_3\text{P}_2$  [49],  $\text{LaN}$  [50],  $\text{Cu}_3\text{PdN}$  [51,52], and  $\text{PbTaSe}_2$  [53].

### ACKNOWLEDGMENTS

H.M.W., Z.F., and X.D. acknowledge the support from the National Natural Science Foundation of China, the 973 program of China (No. 2011CBA00108 and No. 2013CB921700), and the ‘‘Strategic Priority Research Program (B)’’ of the Chinese Academy of Sciences (No. XDB07020100). H.M.W. gratefully acknowledges the hospitality provided during his stay at Tohoku University, where part of this work was performed. Y.K. acknowledges the Russian Megagrant project Grant No. 14.B25.31.0030. Both Y.L. and Y.K. are supported by JST, CREST, ‘‘A mathematical challenge to a new phase of material sciences’’ (2008–2013). Part of the calculations were preformed on TianHe-1(A), the National Supercomputer Center in Tianjin, China.

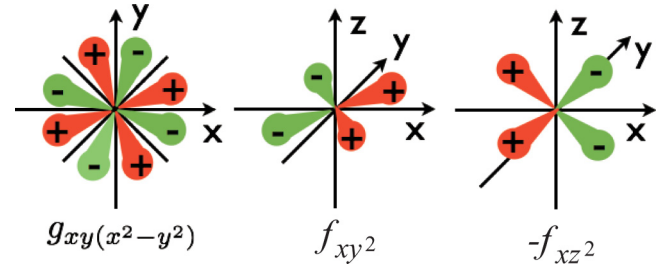


FIG. 5. (Color online) The angular distribution of  $g_{xy(x^2-y^2)}$ ,  $f_{xy^2}$ , and  $-f_{xz^2}$  orbitals.

## APPENDIX A: TIGHT-BINDING MODEL

### 1. 6-1-1-p case

The hypothetic atomic orbital basis set is arranged in the order of  $g_{xy(x^2-y^2)}$ ,  $g_{yz(y^2-z^2)}$ ,  $g_{zx(z^2-x^2)}$ ,  $f_x(y^2-z^2)$ ,  $f_y(z^2-x^2)$ , and  $f_z(x^2-y^2)$ . Those from  $g$  ( $f$ ) orbitals are triply degenerate and the on-site energy is set as  $E_g$  ( $E_f$ ). Due to the cubic symmetry, only the  $g_{xy(x^2-y^2)}$  orbital is plotted in the  $xy$  plane in Fig. 5. The  $f_x(y^2-z^2)$  is plotted as two parts  $f_{xy^2}$  and  $-f_{xz^2}$ , perpendicular to each other. Arranging these orbitals on a simple-cubic lattice with lattice constant  $a$ , the Slater-Koster parameters for nearest-neighbor hopping are defined in the following. The nearest hopping between  $g_{xy(x^2-y^2)}$  in the  $x$  and  $y$  directions is  $V_{ggp}$ , while that in the  $z$  direction is  $V_{ggd}$ . The hopping between  $f_{xy^2}$  ( $-f_{xz^2}$ ) along  $x$  and  $y$  ( $x$  and  $z$ ) is  $V_{ffp}$ , and that along the  $z$  ( $y$ ) direction is  $V_{ffd}$ . The hopping between nearest neighboring  $g_{xy(x^2-y^2)}$  and  $f_{xy^2}$  ( $-f_{xz^2}$ ) along the  $y$  direction is  $V_{fgp}$  ( $V_{fgd}$ ), while that along the  $x$  and  $z$  directions is zero. We list some of the nonzero elements of the final tight-binding Hamiltonian, and others can be easily derived by using the cubic cyclic symmetry,

$$\begin{aligned} H_{g_{xy(x^2-y^2)}, g_{xy(x^2-y^2)}} &= E_g + 2 \cos(\vec{k} \cdot \vec{a}_x) V_{ggp} \\ &\quad + 2 \cos(\vec{k} \cdot \vec{a}_y) V_{ggp} + 2 \cos(\vec{k} \cdot \vec{a}_z) V_{ggd}, \\ H_{g_{xy(x^2-y^2)}, f_{xy^2}} &= i \times 2 \sin(\vec{k} \cdot \vec{a}_y) V_{fgp} + i \times 2 \sin(\vec{k} \cdot \vec{a}_y) V_{fgd}, \\ H_{g_{xy(x^2-y^2)}, f_{yz^2-x^2}} &= i \times 2 \sin(\vec{k} \cdot \vec{a}_x) V_{fgp} + i \times 2 \sin(\vec{k} \cdot \vec{a}_x) V_{fgd}, \\ H_{f_{xy^2}, f_{xy^2}} &= E_f + 2 \cos(\vec{k} \cdot \vec{a}_x) V_{ffp} + 2 \cos(\vec{k} \cdot \vec{a}_x) V_{ffd} \\ &\quad - 2 \cos(\vec{k} \cdot \vec{a}_y) V_{ffp} - 2 \cos(\vec{k} \cdot \vec{a}_y) V_{ffd} \\ &\quad - 2 \cos(\vec{k} \cdot \vec{a}_z) V_{ffp} - 2 \cos(\vec{k} \cdot \vec{a}_z) V_{ffd}. \end{aligned}$$

Here  $\vec{a}_x$ ,  $\vec{a}_y$ , and  $\vec{a}_z$  are the nearest-neighbor sites along the positive  $x$ ,  $y$ , and  $z$  directions, respectively. We have fitted all the Slater-Koster parameters, and we found that  $E_g = -0.12$ ,  $E_f = 0.19$ ,  $V_{ffp} = 0.019$ ,  $V_{ffd} = -0.075$ ,  $V_{fgp} = 0.05$ ,  $V_{fgd} = 0.0$ ,  $V_{ggp} = -0.035$ , and  $V_{ggd} = -0.055$  (all in eV) can well reproduce the band structure from first-principles calculation, as shown in Fig. 2.

However, the following set of parameters will modify the band structure by shifting the band crossing from  $R$ - $M$  to  $\Gamma$ - $M$ . The band structure with  $E_g = -0.10$ ,  $E_f = 0.16$ ,  $V_{ffp} = -0.010$ ,  $V_{ffd} = -0.080$ ,  $V_{fgp} = 0.05$ ,  $V_{fgd} = 0.0$ ,  $V_{ggp} = -0.055$ , and  $V_{ggd} = -0.035$  is shown in Fig. 6. Compared with that in the realistic case, there is additional

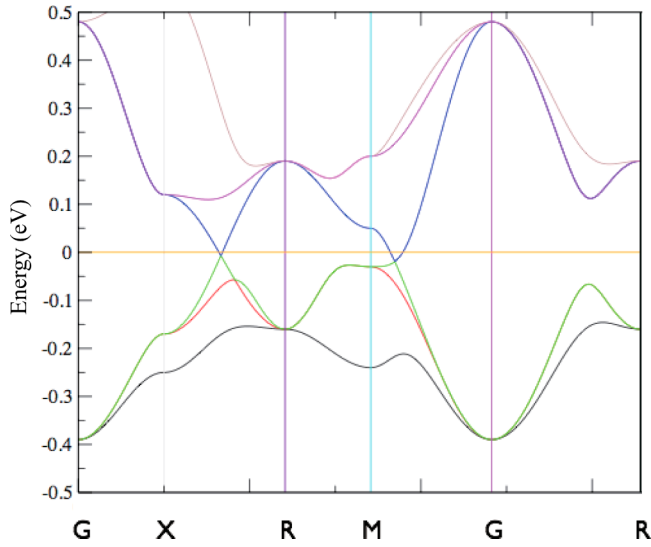


FIG. 6. (Color online) The tight-binding band structure with  $E_g = -0.10$ ,  $E_f = 0.16$ ,  $V_{ffp} = -0.010$ ,  $V_{ffd} = -0.080$ ,  $V_{fgp} = 0.05$ ,  $V_{fgd} = 0.0$ ,  $V_{ggp} = -0.055$ , and  $V_{ggd} = -0.035$ . The band crossing point is shifted from  $R$ - $M$  to  $M$ - $\Gamma$  compared with Fig. 3.

band inversion at  $M$ . This changes the  $Z_2$  index to be  $(0;111)$  if the tiny SOC is considered.

## 2. 6-1-2-p case

For the 6-1-2-p case, the band structure from first-principles calculation is shown in Fig. 7. Obviously, there is band inversion around the  $M$  point. Careful analysis has shown that the occupied and unoccupied triply degenerated bands at  $\Gamma$  (also at the  $R$  point) are  $T_{1u}$  and  $T_{2g}$ , respectively. Therefore, we can take hypothetical  $p_x$ ,  $p_y$ , and  $p_z$  orbitals as the basis

for  $T_{1u}$  representation in cubic symmetry and  $d_{xy}$ ,  $d_{yz}$ , and  $d_{zx}$  as the basis for  $T_{2g}$ . All the  $p$  orbitals have on-site energy  $E_p$  and  $d$  orbitals have  $E_d$ . The Slater-Koster parameters such as  $V_{pp\sigma}$ ,  $V_{pp\pi}$ ,  $V_{dd\pi}$ ,  $V_{dd\delta}$ , and  $V_{pd\pi}$  are defined the same [54]. Putting these orbitals on a simple-cubic lattice, we can have the tight-binding Hamiltonian, and some of the nonzero elements are listed as follows:

$$\begin{aligned} H_{x,x} &= E_p + 2 \cos(\vec{k} \cdot \vec{a}_x) V_{pp\sigma} \\ &\quad + 2 \cos(\vec{k} \cdot \vec{a}_y) V_{pp\pi} + 2 \cos(\vec{k} \cdot \vec{a}_z) V_{pp\pi}, \\ H_{x,xy} &= i \times 2 \sin(\vec{k} \cdot \vec{a}_y) V_{pd\pi}, \\ H_{x,zx} &= i \times 2 \sin(\vec{k} \cdot \vec{a}_z) V_{pd\pi}, \\ H_{xy,xy} &= E_d + 2 \cos(\vec{k} \cdot \vec{a}_x) V_{dd\pi} \\ &\quad + 2 \cos(\vec{k} \cdot \vec{a}_y) V_{dd\pi} + 2 \cos(\vec{k} \cdot \vec{a}_z) V_{dd\delta}. \end{aligned}$$

The other elements can be obtained using cubic cyclic symmetry. The fitted parameters, which can well reproduce the band structure from first-principles calculation, are  $E_p = -0.10147$ ,  $E_d = 0.28281$ ,  $V_{pp\sigma} = 0.02005$ ,  $V_{pp\pi} = -0.017848$ ,  $V_{pd\pi} = 0.034711$ ,  $V_{dd\pi} = 0.04694$ , and  $V_{dd\delta} = -0.062523$ . The mean-square error, around  $0.0061 \text{ eV}^2$ , is estimated for the three conduction bands. Estimation for the valence bands makes the selection of proper bands difficult since there are more than three bands entangled, while the topology of bands from the fitted model is the same as that from first-principles calculation.

## APPENDIX B: REAL-VALUED HAMILTONIAN FOR A SPINLESS SYSTEM WITH BOTH TIME-REVERSAL AND INVERSION SYMMETRY

We will show that for a spinless system with both time-reversal ( $T$ ) and inversion ( $P$ ) symmetry, its Bloch

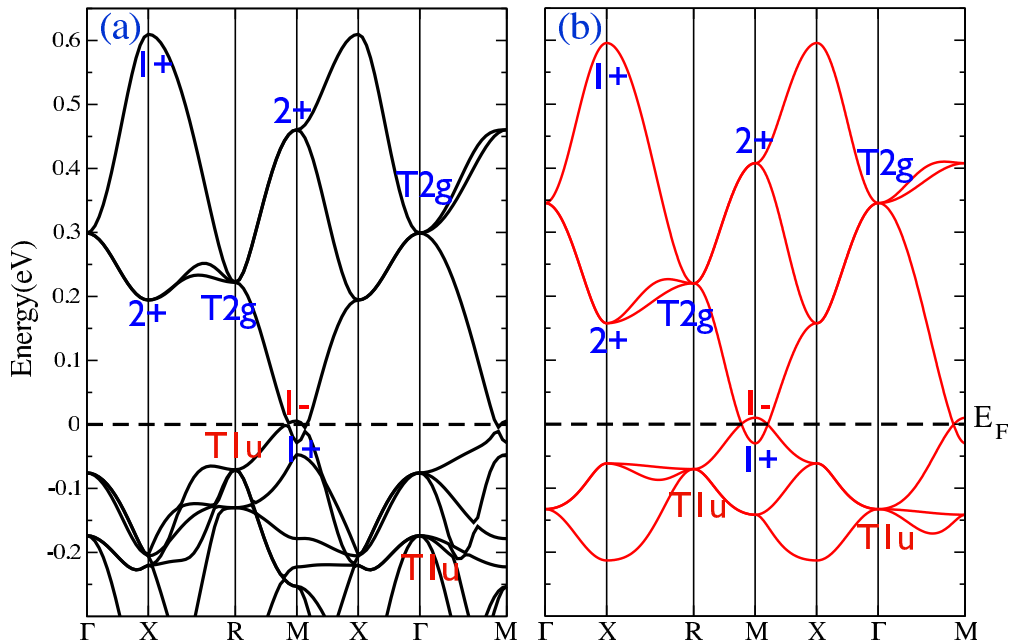


FIG. 7. (Color online) The band structure of the 6-1-2-p case calculated from (a) first-principles and (b) the tight-binding model, respectively. The symmetrical representation, degeneracy, and parity of relevant bands are labeled.

Hamiltonian  $H(\mathbf{k})$  can always be taken as real-valued under a certain gauge choice. In general, plane waves  $e^{i(\mathbf{k}+\mathbf{G}_n)\cdot\mathbf{r}}$  are taken as a basis set to describe  $H(\mathbf{k})$ , where  $\mathbf{G}_n$  are the reciprocal-lattice vectors. With the above chosen basis set, the invariance under the time-reversal operator  $T$  can be expressed as

$$\hat{T}H(\mathbf{k})\hat{T}^{-1} = \hat{O}H^*(\mathbf{k})\hat{O}^{-1} = H(-\mathbf{k})$$

and that of the inversion symmetry reads

$$\hat{O}H(\mathbf{k})\hat{O}^{-1} = H(-\mathbf{k}),$$

where the unitary matrix  $\hat{O}$  can be defined as  $\hat{O}_{nm} = 1$  for  $n = -m$  and zero for all the other matrix elements. From the above two equations, it is obvious that  $H(\mathbf{k})$  is real.

### APPENDIX C: TOPOLOGY OF THE BULK NODE-LINE HAMILTONIAN

As shown in the main text, the effective Hamiltonian for the bulk node-line state can be written as

$$H(k_x, k_y, k_z) = \mathbf{d}(k_x, k_y, k_z) \cdot \boldsymbol{\sigma},$$

where  $\mathbf{d} = (d_x, d_y, d_z)$  and  $\boldsymbol{\sigma} = (\sigma_x, \sigma_y, \sigma_z)$ . Taking  $d_x = k_z$ ,  $d_y = 0$ , and  $d_z = M - B(k_x^2 + k_y^2 + k_z^2)$  can reproduce the bulk node-line state when  $\frac{M}{B} > 0$ . According to Mong *et al.* [47], to check its boundary state on the surface perpendicular to  $k_z$ , this bulk Hamiltonian should be reformulated as

$$\begin{aligned} H(k_{\parallel}, k_z) &= \mathbf{c}_0 + \mathbf{c}_1 k_z + \mathbf{c}_2 k_z^2 \\ &= (0, 0, M - Bk_z^2) + (1, 0, 0)k_z + (0, 0, -B)k_z^2. \end{aligned}$$

Here  $k_{\parallel}$  denotes in-plane coordinates  $(k_x, k_y)$ , and  $\mathbf{c}_0$ ,  $\mathbf{c}_1$ , and  $\mathbf{c}_2$  are vectors in space spanned by  $\boldsymbol{\sigma}$ . The above bulk Hamiltonian is parabolic in the plane spanned by  $\mathbf{c}_1$  and  $\mathbf{c}_2$ . Its origin is within the concave side of the parabola when  $k_{\parallel}(k_x, k_y)$  takes the value satisfying  $k_x^2 + k_y^2 < \frac{M}{B}$ . Thus, there are topologically protected surface states nestled inside of the projected node line with zero eigenenergy to form a “drumhead”-like state.

- 
- [1] H. W. Kroto, J. R. Heath, S. C. O'Brien, R. F. Curl, and R. E. Smalley,  $C_{60}$ : Buckminsterfullerene, *Nature (London)* **318**, 162 (1985).
- [2] S. Iijima, Helical microtubules of graphitic carbon, *Nature (London)* **354**, 56 (1991).
- [3] K. S. Novoselov, A. K. Geim, S. V. Morozov, D. Jiang, Y. Zhang, S. V. Dubonos, I. V. Grigorieva, and A. A. Firsov, Electric field effect in atomically thin carbon films, *Science* **306**, 666 (2004).
- [4] A. K. Geim and K. S. Novoselov, The rise of graphene, *Nat. Mater.* **6**, 183 (2007).
- [5] Y. Yao, F. Ye, X.-L. Qi, S.-C. Zhang, and Z. Fang, Spin-orbit gap of graphene: First-principles calculations, *Phys. Rev. B* **75**, 041401 (2007).
- [6] C. L. Kane and E. J. Mele, Quantum spin Hall effect in graphene, *Phys. Rev. Lett.* **95**, 226801 (2005).
- [7] A. L. Mackay and H. Terrones, Diamond from graphite, *Nature (London)* **352**, 762 (1991).
- [8] R. S. Ruoff, Personal perspectives on graphene: New graphene-related materials on the horizon, *MRS Bull.* **37**, 1314 (2012).
- [9] S. Rajagopalan and R. Robb, Schwarz meets Schwann: Design and fabrication of biomorphic and durataxic tissue engineering scaffolds, *Med. Image Anal.* **10**, 693 (2006).
- [10] T. Lenosky, X. Gonze, M. Teter, and V. Elser, Energetics of negatively curved graphitic carbon, *Nature (London)* **355**, 333 (1992).
- [11] D. Vanderbilt and J. Tersoff, Negative-curvature fullerene analog of  $C_{60}$ , *Phys. Rev. Lett.* **68**, 511 (1992).
- [12] K. Kawasumi, Q. Zhang, Y. Segawa, L. T. Scott, and K. Itami, A grossly warped nanographene and the consequences of multiple odd-membered-ring defects, *Nat. Chem.* **5**, 739 (2013).
- [13] E. Barborini, P. Piseri, P. Milani, G. Benedek, C. Ducati, and J. Robertson, Negatively curved spongy carbon, *Appl. Phys. Lett.* **81**, 3359 (2002).
- [14] K. Nueangnoraj, H. Nishihara, K. Imai, H. Itoi, T. Ishii, M. Kiguchi, Y. Sato, M. Terauchi, and T. Kyotani, Formation of crosslinked-fullerene-like framework as negative replica of zeolite Y, *Carbon* **62**, 455 (2013).
- [15] Y. Ito, Y. Tanabe, H. J. Qiu, K. Sugawara, S. Heguri, N. H. Tu, K. K. Huynh, T. Fujita, T. Takahashi, K. Tanigaki, and M. Chen, High-quality three-dimensional nanoporous graphene, *Ang. Chem.* **126**, 4922 (2014).
- [16] Y. Ito, H.-J. Qiu, T. Fujita, Y. Tanabe, K. Tanigaki, and M. Chen, Bicontinuous nanoporous N-doped graphene for the oxygen reduction reaction, *Adv. Mater.* **26**, 4145 (2014).
- [17] L. Lu, L. Fu, J. D. Joannopoulos, and M. Soljačić, Weyl points and line nodes in gyroid photonic crystals, *Nat. Photon.* **7**, 294 (2013).
- [18] G. P. Mikitik and Yu V. Sharlai, Band-contact lines in the electron energy spectrum of graphite, *Phys. Rev. B* **73**, 235112 (2006).
- [19] G. P. Mikitik and Yu V. Sharlai, The Berry phase in graphene and graphite multilayers, *Low Temp. Phys.* **34**, 794 (2008).
- [20] K. Mullen, B. Uchoa, and D. T. Glatzhofer, Line of Dirac nodes in hyper-honeycomb lattices, [arXiv:1408.5522](https://arxiv.org/abs/1408.5522).
- [21] A. Lherbier, H. Terrones, and J.-C. Charlier, Three-dimensional massless Dirac fermions in carbon schwarzites, *Phys. Rev. B* **90**, 125434 (2014).
- [22] S. A. Yang, H. Pan, and F. Zhang, Dirac and Weyl superconductors in three dimensions, *Phys. Rev. Lett.* **113**, 046401 (2014).
- [23] M. Tagami, Y. Liang, H. Naito, Y. Kawazoe, and M. Kotani, Negatively curved cubic carbon crystals with octahedral symmetry, *Carbon* **76**, 266 (2014).
- [24] <http://www.openmx-square.org>.
- [25] M. Z. Hasan and C. L. Kane, Colloquium: Topological insulators, *Rev. Mod. Phys.* **82**, 3045 (2010).
- [26] X. L. Qi and S. C. Zhang, Topological insulators and superconductors, *Rev. Mod. Phys.* **83**, 1057 (2011).
- [27] L. Fu, C. Kane, and E. Mele, Topological insulators in three dimensions, *Phys. Rev. Lett.* **98**, 106803 (2007).
- [28] A. A. Burkov, M. D. Hook, and Leon Balents, Topological nodal semimetals, *Phys. Rev. B* **84**, 235126 (2011).

- [29] Z. Wang, Y. Sun, X.-Q. Chen, C. Franchini, G. Xu, H. Weng, X. Dai, and Z. Fang, Dirac semimetal and topological phase transitions in  $A_3Bi$  ( $A = Na, K, Rb$ ), *Phys. Rev. B* **85**, 195320 (2012).
- [30] Z. Wang, H. Weng, Q. Wu, X. Dai, and Z. Fang, Three-dimensional Dirac semimetal and quantum transport in  $Cd_3As_2$ , *Phys. Rev. B* **88**, 125427 (2013).
- [31] Z. K. Liu, B. Zhou, Y. Zhang, Z. J. Wang, H. Weng, D. Prabhakaran, S.-K. Mo, Z. X. Shen, Z. Fang, X. Dai, Z. Hussain, and Y. L. Chen, Discovery of a three-dimensional topological Dirac semimetal,  $Na_3Bi$ , *Science* **343**, 864 (2014).
- [32] Z. K. Liu, J. Jiang, B. Zhou, Z. J. Wang, Y. Zhang, H. M. Weng, D. Prabhakaran, S. K. Mo, H. Peng, P. Dudin, T. Kim, M. Hoesch, Z. Fang, X. Dai, Z.-X. Shen, D. L. Feng, Z. Hussain, and Y. L. Chen, A stable three-dimensional topological Dirac semimetal  $Cd_3As_2$ , *Nat. Mater.* **13**, 677 (2014).
- [33] M. Neupane, S.-Y. Xu, R. Sankar, N. Alidoust, G. Bian, C. Liu, I. Belopolski, T.-R. Chang, H.-T. Jeng, H. Lin, A. Bansil, F. Chou, and M. Zahid Hasan, Observation of a three-dimensional topological Dirac semimetal phase in high-mobility  $Cd_3As_2$ , *Nat. Commun.* **5**, 3786 (2014).
- [34] S. Borisenko, Q. Gibson, D. Evtushinsky, V. Zabolotnyy, B. Büchner, and R. J. Cava, Experimental realization of a three-dimensional Dirac semimetal, *Phys. Rev. Lett.* **113**, 027603 (2014).
- [35] Y. Ito and M. Chen (private communication).
- [36] X. Wan, A. M. Turner, A. Vishwanath, and S. Y. Savrasov, Topological semimetal and Fermi-arc surface states in the electronic structure of pyrochlore iridates, *Phys. Rev. B* **83**, 205101 (2011).
- [37] G. Xu, H. Weng, Z. Wang, X. Dai, and Z. Fang, Chern semimetal and the quantized anomalous Hall effect in  $HgCr_2Se_4$ , *Phys. Rev. Lett.* **107**, 186806 (2011).
- [38] G. B. Halász and L. Balents, Time-reversal invariant realization of the Weyl semimetal phase, *Phys. Rev. B* **85**, 035103 (2012).
- [39] A. A. Burkov and L. Balents, Weyl semimetal in a topological insulator multilayer, *Phys. Rev. Lett.* **107**, 127205 (2011).
- [40] S. Ryu and Y. Hatsugai, Topological origin of zero-energy edge states in particle-hole symmetric systems, *Phys. Rev. Lett.* **89**, 077002 (2002).
- [41] T. T. Heikkilä and G. E. Volovik, Dimensional crossover in topological matter: Evolution of the multiple Dirac point in the layered system to the flat band on the surface, *JETP Lett.* **93**, 59 (2011).
- [42] T. T. Heikkilä, N. B. Kopnin, and G. E. Volovik, Flat bands in topological media, *JETP Lett.* **94**, 233 (2011).
- [43] G. E. Volovik, *Topology of Quantum Vacuum*, Lecture Notes in Physics Vol. 870 (Springer, Berlin, 2013), pp. 343–383.
- [44] H. Weng, X. Dai, and Z. Fang, Exploration and prediction of topological electronic materials based on first-principles calculations, *MRS Bull.* **39**, 849 (2014).
- [45] N. B. Kopnin, T. T. Heikkilä, and G. E. Volovik, High-temperature surface superconductivity in topological flat-band systems, *Phys. Rev. B* **83**, 220503 (2011).
- [46] G. E. Volovik, From standard model of particle physics to room-temperature superconductivity, [arXiv:1409.3944](https://arxiv.org/abs/1409.3944).
- [47] R. S. K. Mong and V. Shivamoggi, Edge states and the bulk-boundary correspondence in Dirac Hamiltonians, *Phys. Rev. B* **83**, 125109 (2011).
- [48] Y. Chen, Y. Xie, S. A. Yang, H. Pan, F. Zhang, M. L. Cohen, and S. Zhang, Spin-orbit-free Weyl-loop and Weyl-point semimetals in a stable three-dimensional carbon allotrope, [arXiv:1505.02284](https://arxiv.org/abs/1505.02284).
- [49] L. S. Xie, L. M. Schoop, E. M. Seibel, Q. D. Gibson, W. Xie, and R. J. Cava, Potential ring of Dirac nodes in a new polymorph of  $Ca_3P_2$ , [arXiv:1504.01731](https://arxiv.org/abs/1504.01731) [cond-mat.mtrl-sci].
- [50] M. Zeng, C. Fang, G. Chang, Y.-A. Chen, T. Hsieh, A. Bansil, H. Lin, and L. Fu, Topological semimetals and topological insulators in rare earth mononpnictides, [arXiv:1504.03492](https://arxiv.org/abs/1504.03492) [cond-mat.mes-hall].
- [51] Y. Kim, B. J. Wieder, C. L. Kane, and A. M. Rappe, Dirac line nodes in inversion symmetric crystals, [arXiv:1504.03807](https://arxiv.org/abs/1504.03807) [Phys. Rev. Lett. **114** (2015) (to be published)].
- [52] R. Yu, H. Weng, Z. Fang, X. Dai, and X. Hu, Topological node-line semimetal and Dirac semimetal state in antiperovskite  $Cu_3PdN$ , [arXiv:1504.04577](https://arxiv.org/abs/1504.04577) [Phys. Rev. Lett. **114** (2015) (to be published)].
- [53] G. Bian, T.-R. Chang, R. Sankar, S.-Y. Xu, H. Zheng, T. Neupert, C.-K. Chiu, S.-M. Huang, G. Chang, I. Belopolski, D. S. Sanchez, M. Neupane, N. Alidoust, C. Liu, B. Wang, C.-C. Lee, H.-T. Jeng, A. Bansil, F. Chou, H. Lin, and M. Zahid Hasan, Topological nodal-line fermions in the non-centrosymmetric superconductor compound  $PbTaSe_2$ , [arXiv:1505.03069](https://arxiv.org/abs/1505.03069) [cond-mat.mes-hall].
- [54] J. C. Slater and G. F. Koster, Simplified lcao method for the periodic potential problem, *Phys. Rev.* **94**, 1498 (1954).